## PAPER

# Anisotropic ion diffusion in α-Cr$_2$O$_3$: an atomistic simulation study

Penghui Cao,[a] Daniel Wells[b] and Michael Philip Short*[a]

Chromia (α-Cr$_2$O$_3$) is one of the most technologically important oxides, as it is the basis behind the passivation of many structural materials like stainless steel. It both resists oxygen ingress and slows the release of metals from its substrate by its high density and very low diffusivities. Were any further improvement to the protectiveness of chromia to be realized, no matter how small, it would have an enormous impact due to its ubiquitousness. Here we use molecular dynamics (MD) in conjunction with nudged elastic band (NEB) calculations to study the diffusion mechanisms of oxygen and chromium ions in α-Cr$_2$O$_3$. Significant anisotropic diffusion between the *ab*-plane and the *c*-axis is observed for both oxygen and chromium ions. We found that vacancy-mediated ion diffusion in the *ab*-plane is faster than diffusion along the *c*-axis, while interstitial-mediated diffusion along the *c*-axis is faster. Vacancy and interstitial defect migration paths unveil the atomistic mechanisms responsible for this anisotropic ion diffusion, as the most energetically favorable diffusion path accounts for the observed anisotropy. The results of this study have profound implications for the reduction and control of corrosion.

## 1 Introduction

Chromium oxide (α-Cr$_2$O$_3$) is arguably one of the world's most important oxides. It functions as the protective layer of the world's most utilized corrosion-resistant, structural material, stainless steel. Currently the production of α-Cr$_2$O$_3$-passivated stainless steels continues to grow exponentially, reaching 41.7 million metric tons in 2014,[1] underpinning critical infrastructures ranging from bridges, to buildings, to nuclear reactors. Therefore, any deterministic ways of slowing the progress of oxygen penetration from the environment into the metal, or conversely of metal escape into the environment, would constitute a substantial reduction in the total cost of corrosion worldwide.

For passivating materials that function as effective diffusion barriers,[2] any anisotropy in diffusivity will help to determine the relative, texture-dependent corrosion rates through these materials. Examples of anisotropic cation and anion diffusion through non-cubic oxides exist throughout the literature. These will be reviewed briefly here, with emphasis on those that explore the diffusion mechanisms, not just the rates, behind cation and anion transport. Chroneos *et al.* showed preferential oxygen diffusion in the *a*–*b* plane of tetragonal La$_2$NiO$_{4+\delta}$ using molecular dynamics (MD) simulations, which explained formerly anomalous experimental measurements that varied by a factor of up to 4.5.[3] Kendrick *et al.* showed the importance of mechanistic

understanding in predicting the diffusivity of oxygen in Ga-based oxides, with their results agreeing well with experiments.[4] The critical importance of understanding the diffusion mechanisms through anisotropic oxides in the form of solid oxide fuel cells was recently highlighted by Chroneos *et al.*,[5] underscoring the need for more than the standard experiments or simulations showing simply gross rates of transport without explanation.

The transport of cations and anions specifically through α-Cr$_2$O$_3$ has been experimentally measured[6–13] and simulated,[14–16] though to a degree far lower than would be expected given its technological importance. The experimental literature is more extensive, as tracer experiments of oxygen and cation transport have been performed by multiple groups. Hagel experimentally found that anion diffusion is slower in α-Cr$_2$O$_3$ compared to cation diffusion.[6] Sabioni *et al.* studied the diffusion of oxygen,[7] manganese,[8] chromium,[9] and iron[10] through chromia polycrystals and thin films by secondary ion mass spectroscopy (SIMS), eventually finding that oxygen diffusivity is faster than that of chromium in α-Cr$_2$O$_3$, in conflict with Hagel's results. Lobnig *et al.* also used tracer experiments to study the diffusion of Cr, Fe, and Ni through α-Cr$_2$O$_3$[11] as a function of time, while Tsai *et al.*[12] and Hoshino *et al.*[13] experimentally studied the mechanisms of diffusion of Cr and O through α-Cr$_2$O$_3$. The literature concerning simulations of ionic transport through Cr$_2$O$_3$ are surprisingly scarce, though studies of the surface structure are more common. Catlow *et al.*,[14] Lebreau *et al.*,[15] and Vaari[16] have predicted diffusion coefficients of cations and anions through α-Cr$_2$O$_3$ with comparisons to experimental values, showing mixed results. Because α-Cr$_2$O$_3$ has a hexagonal close-packed (HCP)

[a] Department of Nuclear Science and Engineering, Massachusetts Institute of Technology, Cambridge, MA, USA. E-mail: hereiam@mit.edu

[b] Electric Power Research Institute, Charlotte, NC, USA

crystal structure with a $c/a$ axis ratio of 2.74 over a very wide pressure range,[17] any application utilizing $\alpha$-$Cr_2O_3$ as a passivation layer, from near-vacuum to ultra-high pressure, should benefit from the same texture-based gains in transport resistance. Therefore, precise knowledge of the orientation-dependent transport rates determines whether this strategy can succeed.

In this work, we present the orientation-dependent diffusivities of oxygen and chromium ions through $\alpha$-$Cr_2O_3$, and describe specific, anisotropic transport mechanisms. A combination of MD simulations and nudged elastic band (NEB) calculations of minimum energy pathways shows clear, temperature-dependent anisotropy in diffusion. The anisotropy observed for both oxygen and chromium, which increases at lower temperatures, points to potentially enhanced corrosion resistance of $\alpha$-$Cr_2O_3$ grown with the $c$-axis perpendicular to the material surface. Such a finding has large implications for corrosion resistance, should a method be developed which induces the growth of properly textured $\alpha$-$Cr_2O_3$.

## 2 Methodology

Like $\alpha$-$Al_2O_3$ and $\alpha$-$Fe_2O_3$, $\alpha$-$Cr_2O_3$ has the corundum structure shown in Fig. 1, with hexagonally close-packed oxygen anions. In this structure, chromium cations occupy two thirds of the available octahedral sites, and interstitial sites exist between alternative pairs of cations. To properly model this oxide system, we combine a short range Buckingham potential and a long range Coulombic term to model ionic interactions. The potential for the interaction between two ions $i$ and $j$ at a distance $r$ is defined by eqn (1):

$$U_{ij}(r) = A_{ij}e^{\frac{-r}{\rho_{ij}}} - \frac{C_{ij}}{r_{ij}} + \frac{q_i q_j}{4\pi\varepsilon_0 r_{ij}} \qquad (1)$$

where the parameters $A$, $\rho$, and $C$ are taken from the previous studies of Grimes et al.[18] This potential was parameterized with reference to experimental data and it was shown to successfully predict lattice parameters, defect formation and activation energies, and bulk diffusion.[3,16,19–21]
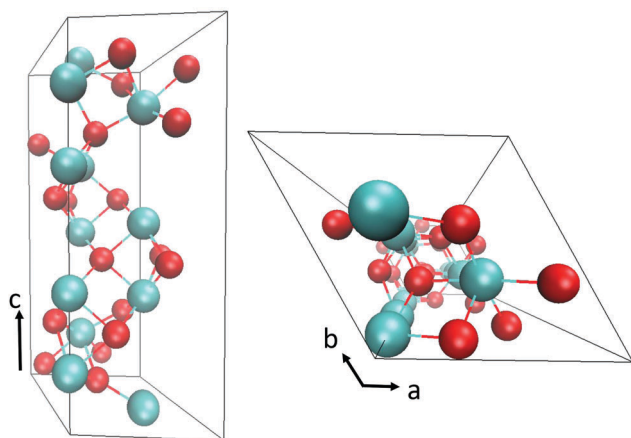


**Fig. 1** Schematic of the $\alpha$-$Cr_2O_3$ hexagonal unit cell used in the simulations of this study. The arrows show the $c$-axis and the $ab$-plane. Cr atoms are colored in blue, while O atoms are in red.

MD simulations are carried out in bulk $\alpha$-$Cr_2O_3$ containing $18 \times 18 \times 18$ hexagonal supercells (58320 atoms) with periodic boundary conditions applied in all three directions. We use the Particle–Particle Particle–Mesh (PPPM) method[22] to compute the long range Coulombic interaction component of eqn (1), and the short-range part of the potential is calculated with a cutoff distance of 10 Å. The Nose–Hoover thermostat[23,24] is used in time integration with a time-step of 1 fs. To study vacancy- and interstitial-assisted ion diffusion, atoms are randomly removed from or inserted into the system according to stoichiometry such that the total charge of the system is zero. We studied ion diffusion at point defect (vacancy, interstitial) concentrations of 0.04% and 0.08%, and found that the diffusion anisotropy does not depend on the studied concentrations. The results reported in this paper are obtained from studies with a defect concentration of 0.08%.

We relax the atomic structure at zero pressure for 0.1 ns in the *NPT* (constant number of atoms, pressure, and temperature) ensemble, and another 0.1 ns relaxation is performed in the *NVT* ensemble (constant number of atoms, volume, and temperature). After that, the diffusivity of each ion is determined by measuring its mean square displacement (MSD) as a function of time in an extensive, 1 ns long *NVT* simulation. The calculation of the MSD is described by eqn (2):

$$\langle \Delta r^2(t) \rangle = \frac{1}{N}\sum_{i=1}^{N}[r_i(t+t_0) - r_i(t_0)]^2 \qquad (2)$$

where ($N$) is the total number of ions in the system, $r(t_0)$ represent the initial reference positions at time $t_0$, and $r(t)$ are the positions at time $t_0 + t$. The diffusivity that relates the MSD to the observed time ($t$) is defined in eqn (3):

$$D = \frac{\langle r^2(t) \rangle}{2d \times t} \qquad (3)$$

where $d$ is the diffusion dimensionality. The diffusivities along the $c$-axis, in the $ab$-plane, and in the three dimensions (3d) can be calculated by $D_c = \langle r_c^2(t) \rangle/2t$, $D_{ab} = \langle r_{ab}^2(t) \rangle/4t$ and $D_{3d} = \langle r_{abc}^2(t) \rangle/6t$, respectively. To ensure adequate statistical sampling, four independent diffusion simulations are performed for each case in this work. Next, NEB[25,26] calculations are performed to compute the minimum energy migration barriers for ions traveling on each diffusion pathway, and 20 replicas are constructed and computed along each migration trajectory.

All MD simulations and NEB calculations are performed using the LAMMPS software package.[27] The LAMMPS simulation input files, output files, raw data, and processing scripts are hosted permanently on our GitHub public repository.[28]

## 3 Results

### 3.1 Temperature dependence of ion diffusion

**3.1.1 Ion diffusion *via* vacancies (vacancy-mediated).** We report in Fig. 2(a) the calculated 3d vacancy diffusion coefficients of chromium and oxygen at temperatures ranging from 1300 K to 2000 K. The error bars in Fig. 2 present one standard deviation
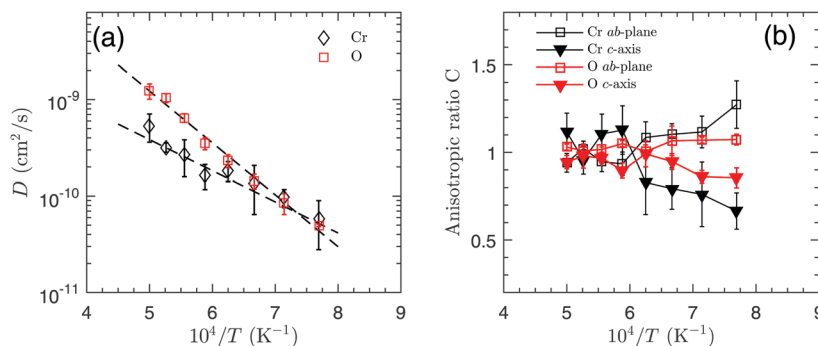
Fig. 2 (a) Vacancy-mediated diffusion coefficients of oxygen and chromium as functions of temperature. Dashed lines are Arrhenius fits. (b) Diffusion anisotropy ratio $C$ in the $ab$-plane and along the $c$-axis, showing increased anisotropy at lower temperatures.

of the coefficients measured from four independent simulations. One can see that both oxygen and chromium diffusion follow the typical Arrhenius behavior within the temperature range of this investigation. It is worth noting that oxygen diffuses much faster than chromium at temperatures above 1500 K, while at low temperatures chromium shows a larger diffusion coefficient. The faster oxygen anion diffusion at high temperatures obtained in the simulations agrees with previous experimental measurements.[9,10]

To quantify diffusional anisotropy in the $ab$-plane and along the $c$-axis, we define a relative diffusion ratio $C$, calculated as $D_{ab}/D_{3d}$ and $D_c/D_{3d}$, where $D_{ab}$ and $D_c$ are diffusion coefficients in the $ab$-plane and along the $c$-axis, respectively, and $D_{3d}$ is the 3d diffusion coefficient plotted in Fig. 2(a). Clear evidence of anisotropic diffusion can be seen in Fig. 2(b), where we plot the anisotropic ratios as a function of temperature, $10^4/T$. We observe that both oxygen and chromium show higher in-plane diffusivities at temperatures below 1500 K, with the effect more extreme for the case of Cr diffusion. At 1300 K ($10^4/T$ = 7.69), chromium in-plane diffusion is 1.9 times larger than $c$-axis diffusion. The diffusion anisotropy $C$ trends towards unity as the temperature increases, and vacancy diffusion becomes directionally independent at temperatures higher than 1700 K (isotropic diffusion). The observed anisotropic diffusion will be further addressed using details to follow from the vacancy diffusion pathway analysis section.

**3.1.2 Ion diffusion *via* interstitials (interstitial-mediated).** The computed 3d interstitial diffusion coefficients of chromium and oxygen at temperatures ranging from 1200 K to 2000 K are shown in Fig. 3(a). In comparison with vacancy diffusion, interstitials usually exhibit higher mobilities due to smaller migration barriers. This is the case when we compare Fig. 2(a) and 3(a), where it can be seen that interstitial diffusion is much faster than vacancy diffusion for both oxygen and chromium. Unlike the temperature dependence of the anisotropy ratio in vacancy diffusion, the interstitial anisotropy ratio $C$ only depends weakly on temperature. We find at all studied temperatures that the interstitial transport along the $c$-axis is the primary diffusion process: axial chromium diffusion is thirty times faster than in-plane diffusion, and oxygen diffusivity is 1.4 times higher along the $c$-axis.

### 3.2 Vacancy and interstitial diffusion paths

To further investigate anisotropic ion diffusion observed in the previous section, and to understand the underlying ion transport mechanisms, we have analyzed energetically possible defect diffusion paths and compared the corresponding migration energies.

**3.2.1 Oxygen vacancy migration paths.** In these simulations, a single oxygen atom from the lattice site is selected and removed to create a vacancy. Five unique vacancy migration paths are identified involving the first and second nearest oxygen neighbors, as shown in Fig. 4. Since oxygen ions are hexagonally
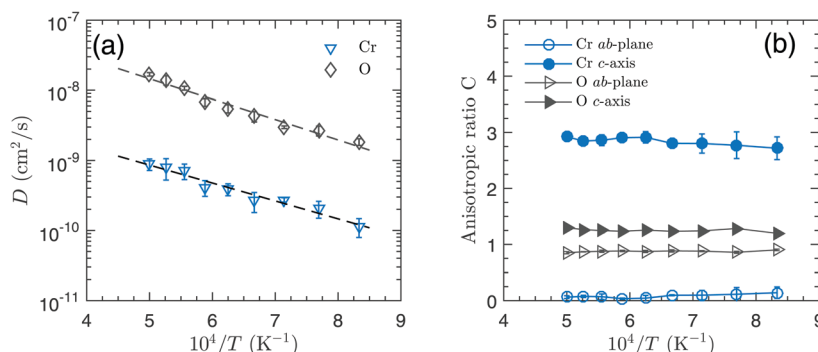


Fig. 3 (a) Interstitial-mediated diffusion coefficients of oxygen and chromium as functions of temperature. Dashed lines are Arrhenius fits. (b) Diffusion anisotropy ratio $C$ in the $ab$-plane and along the $c$-axis.
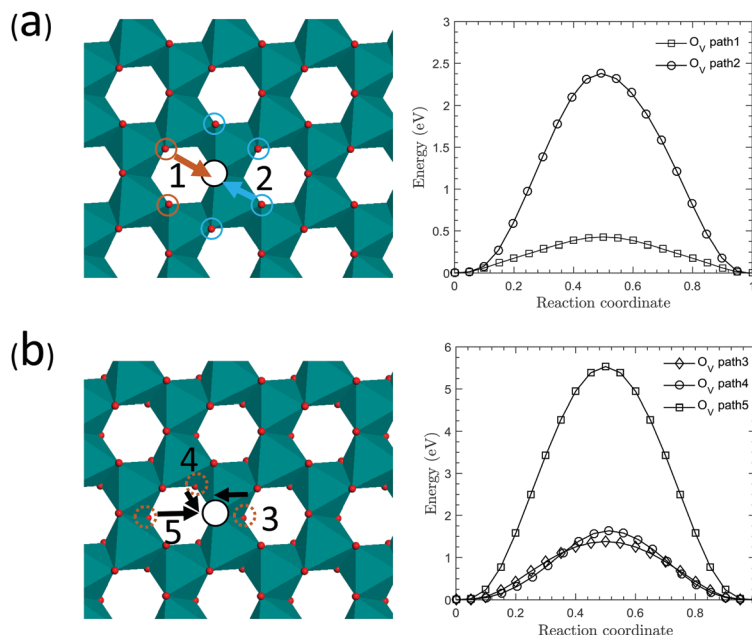
**Fig. 4** Oxygen vacancy migration paths and corresponding energy barriers. The left panels demonstrate oxygen vacancy diffusion paths: (a) in the *ab*-plane, (b) out of plane. Small red balls represent oxygen, the black circle is a vacancy, and octahedra are colored in green. The right panels show minimum energy barriers for the migration trajectories, calculated by the NEB method.

close-packed, one vacancy has six nearest neighbors on the *a–b* plane. Due to this structural symmetry, only two of the six paths, $O_v$-1 and $O_v$-2, are considered to be distinct. The paths $O_v$-1 and $O_v$-2 highlighted in Fig. 4(a) are confined to the plane. The path of $O_v$-2 occurs between two oxygen sites sharing the same octahedron, whereas $O_v$-1 involves an oxygen site on a neighboring octahedral vertex. The other three diffusion paths involving out-of-plane diffusion, $O_v$-3, $O_v$-4, and $O_v$-5, are shown in Fig. 4(b). The out-of-plane diffusion paths occur either by moving along an octahedral edge ($O_v$-3, $O_v$-4) or by passing through a chromium interstitial site ($O_v$-5). The difference between $O_v$-3 and $O_v$-4 is that the path of $O_v$-3 is shared by two octahedra, while that of $O_v$-4 is not. The minimum migration energy barriers for each diffusion path are calculated by using the NEB method with 20 replicas, and are shown on the right panel of Fig. 4. We report in Table 1 the values of oxygen migration energies $E_m$, in-plane jump distances $d_{ab}$, and axial jump distances $d_c$. The path of $O_v$-1 that only involves in-plane migration has the lowest energy barrier of 0.425 eV. It is known from transition state theory that the migration frequency $v$ depends on the migration barrier $E_m$ according to the formula $v = v_0 e^{-E_m/k_B T}$, where $v_0$ is the attempt frequency, $k_B$ is Boltzmann's constant, and $T$ is the

system temperature. When the temperature is low, the low energy paths $O_v$-1 and $O_v$-2 are energetically favorable and *ab*-plane diffusional migrations are significantly active. These asymmetric vacancy pathways are related to the anisotropic diffusion results shown in Fig. 2.

**3.2.2 Chromium vacancy migration paths.** We propose five energetically possible, distinct migration paths for chromium vacancies by considering neighboring chromium sites. The paths of $Cr_v$-1, $Cr_v$-2, and $Cr_v$-3 involve diffusion within the chromium bilayer contained within the *ab*-plane shown in Fig. 5(a), where $Cr_v$-1 relates to a jump between nearest neighbor chromium sites, and $Cr_v$-2 and $Cr_v$-3 involve the second and third nearest neighbors within a chromium cation bilayer. The calculated migration energies in Fig. 5(a) show that the migration barriers of $Cr_v$-2 and $Cr_v$-3 are much greater than that of $Cr_v$-1. The other two paths $Cr_v$-4 and $Cr_v$-5 only transport chromium along the *c*-axis. Path $Cr_v$-4 relates to migration between two neighboring chromium sites while $Cr_v$-5 involves movement through a chromium interstitial site. We note that the energy path of $Cr_v$-5 in Fig. 5(b) displays an intermediate state, which corresponds to vacancy migration into the interstitial site. Table 2 reports the calculated migration energies and jump distances for chromium vacancies. The high *ab*-plane vacancy diffusivity of chromium is attributed to the low migration energy path $Cr_v$-1 which involves a large in-plane jump distance $d_{ab}$.

**3.2.3 Chromium interstitial migration paths.** Chromium interstitial migration is studied by inserting a chromium ion into an unoccupied octahedral hole. An interesting cascade-like diffusion mechanism is found, as shown in Fig. 6. Three chromium ions on the *c*-axis, two of which are neighboring chromium ions and one is an interstitial, are involved in the migration and

**Table 1** Migration energy $E_m$, plane jump distance $d_{ab}$, and axial jump distance $d_c$ for oxygen vacancy diffusion mechanisms

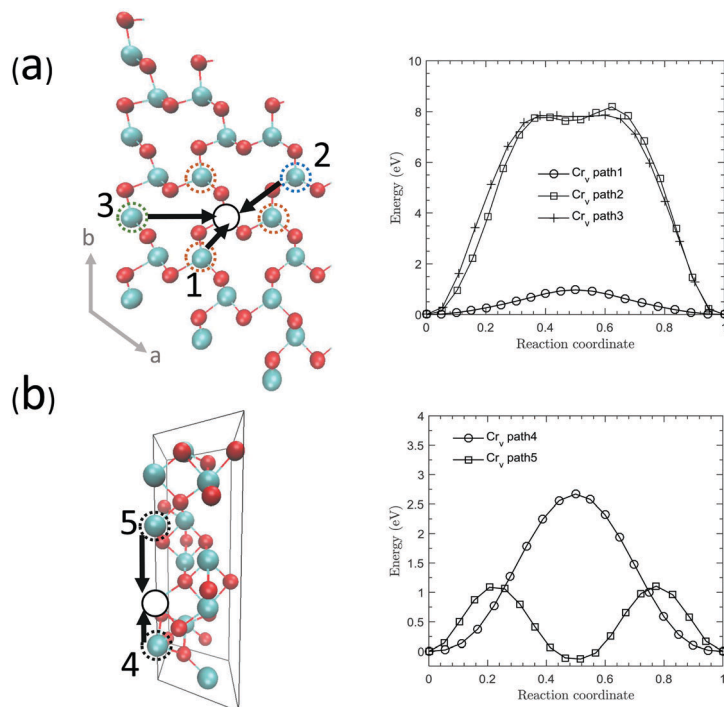| Path | $E_m$ (eV) | $d_{ab}$ (Å) | $d_c$ (Å) |
|---|---|---|---|
| $O_v$-1 | 0.425 | 2.63 | 0 |
| $O_v$-2 | 2.38 | 2.99 | 0 |
| $O_v$-3 | 1.38 | 1.53 | 2.27 |
| $O_v$-4 | 1.63 | 1.72 | 2.27 |
| $O_v$-5 | 5.53 | 3.45 | 2.27 |

**Fig. 5** Chromium vacancy migration paths and corresponding energy barriers. The left panels demonstrate chromium vacancy diffusion paths: (a) in the *ab*-plane, (b) out-of-plane along the *c*-axis. The right panels show minimum energy barriers for the migration trajectories calculated by the NEB method.

**Table 2** Migration energy $E_m$, plane jump distance $d_{ab}$, and axial jump distance $d_c$ for chromium vacancy diffusion mechanisms

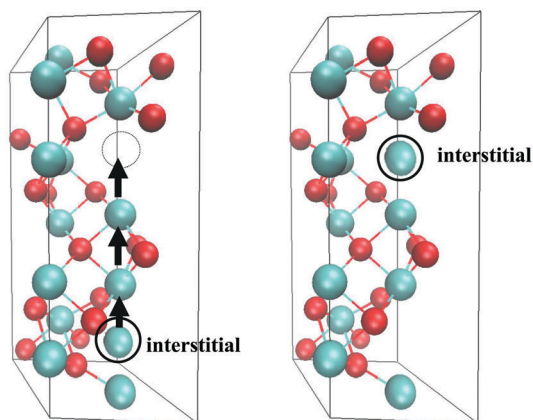| Path | $E_m$ (eV) | $d_{ab}$ (Å) | $d_c$ (Å) |
|---|---|---|---|
| $Cr_v$-1 | 0.971 | 2.84 | 0.385 |
| $Cr_v$-2 | 8.19 | 4.96 | 0 |
| $Cr_v$-3 | 7.86 | 5.73 | 0.385 |
| $Cr_v$-4 | 2.67 | 0 | 2.65 |
| $Cr_v$-5 | 1.23 | 0 | 6.41 |



**Fig. 6** The cascade-like chromium interstitial diffusion mechanism. The left figure shows the atomic configuration before an interstitial migration transition, and the right figure shows the structure following migration.

transport of interstitials in a coordinated manner. This cascade-like diffusion process with a low migration energy of 1.37 eV accounts for the dominant *c*-axis chromium interstitial diffusion.

# 4 Discussion

The results in this study show clearly anisotropic diffusion of both cations and anions in $\alpha$-$Cr_2O_3$, by both vacancy and interstitial mechanisms. Both oxygen and chromium are known to diffuse primarily by the vacancy mechanism, the anisotropy of which varies considerably with temperature. Therefore, the discussion will be mostly limited to the obtained values and implications of vacancy diffusivity for both cations and anions.

The results in this study, in addition to having major implications for even minor potential reductions in oxidation rates, may specifically apply to slowing the release of metal cations into working fluids in energy systems. The protective oxide in fluid mass transport systems, such as those transporting water in heat exchangers or nuclear reactors, acts as the primary barrier to metal release into the system's working fluid. These cations can reach supersaturation in the coolant, growing additional oxide crystals which detach due to fluid shear, eventually forming fouling deposits throughout energy systems. Fouling alone costs industrialized nations 0.25% of their gross domestic product (GDP) per year, which amounts to $42 billion in the US in 2013,[29] and it could be partially prevented by slowing metal release through such protective oxides. Should a method exist to induce chromia film growth with the *c*-axis normal to the material surface, it would represent a small change to manufacturing processes that could slow both corrosion and the release of foulants with no chemical or structural change to the materials involved.

Such a method to induce textured $\alpha$-$Cr_2O_3$ may exist in the realm of elastic strain engineering,[30] whereby the material

properties and even textures are intentionally altered by elastically straining the underlying substrate. One particularly relevant success of elastic strain engineering has been demonstrated: the increase in carrier mobility in Si by factors of 3–5.[31] Modifying the materials on which $\alpha$-Cr$_2$O$_3$ grows, either by straining them or adding a very thin buffer layer to create strain, may induce texture-dependent oxide growth, as has been seen for nano-composite films grown on *c*-axis sapphire.[32] In fact, greatly differing oxidation rates for nuclear steam generator tubes, made from the same alloy, have been observed between manufacturing processes[33] that result in a pre-strained or annealed condition. This suggests that certain processes, which result in surface strain of the underlying metal, could induce textured $\alpha$-Cr$_2$O$_3$ formation with slower metal release or oxidation. The required combination of structure, orientation, and strain can now be dynamically studied during growth,[34] allowing for faster determination whether a particular technique induces textured $\alpha$-Cr$_2$O$_3$ growth.

## 5 Conclusions

Atomistic simulations of vacancy- and interstitial-mediated ion diffusion in $\alpha$-Cr$_2$O$_3$ showed considerable anisotropy. Vacancy-mediated diffusion, which is the dominant mode of mass transport through $\alpha$-Cr$_2$O$_3$, is faster in the *ab*-plane below 1600 K, while ion diffusion along the *c*-axis is the faster process for interstitial diffusion. The computed ion diffusion agrees with previous experimental findings, and diffusional anisotropy is predicted to have a larger effect at lower temperatures. This finding has critical implications for new methods to slow both corrosion and metal release which would lead to fouling in energy systems, as even small reductions in transport by inducing a preferred $\alpha$-Cr$_2$O$_3$ texture (the *c*-axis normal to the substrate surface) would have a large impact on global corrosion and fouling due to the ubiquitousness of $\alpha$-Cr$_2$O$_3$ as a protective oxide layer. Strategies for inducing this texture, as well as ways of confirming its effectiveness, are suggested as follow-on work to realize these computationally-predicted gains.

## Acknowledgements

## References

1 I. S. S. F. (ISSF), Stainless Steel in Figures: 2015, International stainless steel forum (issf) technical report, 2015.
2 D. A. Jones, *Principles and prevention of corrosion*, Prentice Hall, 2nd edn, 1996.
3 A. Chroneos, D. Parfitt, J. A. Kilner and R. W. Grimes, *J. Mater. Chem.*, 2010, **20**, 266–270.
4 E. Kendrick, J. Kendrick, K. S. Knight, M. S. Islam and P. R. Slater, *Nat. Mater.*, 2007, **6**, 871–875.
5 A. Chroneos, B. Yildiz, A. Tarancon, D. Parfitt and J. A. Kilner, *Energy Environ. Sci.*, 2011, **4**, 2774–2789.
6 W. C. Hagel, *J. Am. Ceram. Soc.*, 1965, **48**, 70–75.
7 A. C. S. Sabioni, A. M. Huntz, F. Millot and C. Monty, *Philos. Mag. A*, 1992, **66**, 351–360.
8 A. Sabioni, A. Huntz, F. Silva and F. Jomard, *Mater. Sci. Eng., A*, 2005, **392**, 254–261.
9 A. C. S. Sabioni, R. P. B. Ramos, V. Ji, F. Jomard, W. A. de Almeida Macedo, P. L. Gastelois and V. B. Trindade, *Oxid. Met.*, 2012, **78**, 211–220.
10 A. C. S. Sabioni, A. M. Huntz, L. C. Borges and F. Jomard, *Philos. Mag.*, 2007, **87**, 1921–1937.
11 R. Lobnig, H. Schmidt, K. Hennesen and H. Grabke, *Oxid. Met.*, 1992, **37**, 81–93.
12 S. Tsai, A. Huntz and C. Dolin, *Mater. Sci. Eng., A*, 1996, **212**, 6–13.
13 K. Hoshino and N. Peterson, *J. Am. Ceram. Soc.*, 1983, **66**, c202–c203.
14 C. R. A. Catlow, J. Corish, J. Hennessy and W. C. Mackrodt, *J. Am. Ceram. Soc.*, 1988, **71**, 42–49.
15 F. Lebreau, M. M. Islam, B. Diawara and P. Marcus, *J. Phys. Chem. C*, 2014, **118**, 18133–18145.
16 J. Vaari, *Solid State Ionics*, 2015, **270**, 10–17.
17 L. W. Finger and R. M. Hazen, *J. Appl. Phys.*, 1980, **51**, 5362–5367.
18 L. Minervini, R. W. Grimes, J. A. Kilner and K. E. Sickafus, *J. Mater. Chem.*, 2000, **10**, 2349–2354.
19 R. W. Grimes, D. J. Binks and A. B. Lidiard, *Philos. Mag. A*, 1995, **72**, 651–668.
20 L. Minervini, M. O. Zacate and R. W. Grimes, *Solid State Ionics*, 1999, **116**, 339–349.
21 D. Parfitt, A. Chroneos, J. A. Kilner and R. W. Grimes, *Phys. Chem. Chem. Phys.*, 2010, **12**, 6834–6836.
22 R. W. Hockney and J. W. Eastwood, *Computer simulation using particles*, CRC Press, 1988.
23 W. G. Hoover, *Phys. Rev. A*, 1985, **31**, 1695.
24 S. Nosé, *Mol. Phys.*, 1984, **52**, 255–268.
25 G. Henkelman, B. P. Uberuaga and H. Jónsson, *J. Chem. Phys.*, 2000, **113**, 9901–9904.
26 G. Henkelman and H. Jónsson, *J. Chem. Phys.*, 2000, **113**, 9978–9985.
27 S. Plimpton, *J. Comput. Phys.*, 1995, **117**, 1–19.
28 https://github.com/shortlab/2016Cr2O3.
29 H. Müller-Steinhagen and A. P. Watkinson, *Heat Transfer Eng.*, 2005, **26**, 1–4.
30 J. Li, Z. Shan and E. Ma, *MRS Bull.*, 2014, **39**, 108–114.
31 C. S. Smith, *Phys. Rev.*, 1954, **94**, 42.
32 A. Chen, M. Weigand, Z. Bi, W. Zhang, X. Lü, P. Dowden, J. L. MacManus-Driscoll, H. Wang and Q. Jia, *Sci. Rep.*, 2014, **4**, 5426.
33 C. Marks, M. Little, P. Krull, D. Hussey and K. Epperson, *NPC 2012: Nuclear Plant Chemistry Conference*, France, 2012.
34 J. D. Budai, W. Yang, N. Tamura, J.-S. Chung, J. Z. Tischler, B. C. Larson, G. E. Ice, C. Park and D. P. Norton, *Nat. Mater.*, 2003, **2**, 487–492.